CHEMISTRY
A European Journal

A Journal of
ChemPubSoc Europe

Accepted Article

Title: Microscopic Insights on the Multiferroic Perovskite-like [CH3NH3][Co(COOH)3] Compound

Authors: Lidia Mazzuca, Laura Canadillas-Delgado, Oscar Fabelo, J. Al berto Rodriguez-Velamazan, Javier Luzon, Oriol Vallcorba, Virginie Simonet, Claire V. Colin, and Juan Rodriguez-Carvajal

To be cited as: *Chem. Eur. J.* 10.1002/chem.201703140

Link to VoR: http://dx.doi.org/10.1002/chem.201703140

Supported by ACES

WILEY-VCH

Microscopic Insights on the Multiferroic Perovskite-like $[CH_3NH_3][Co(COOH)_3]$ Compound

Lidia Mazzuca,[a] Laura Cañadillas-Delgado,* [a, b] Oscar Fabelo,*[a] J. Alberto Rodríguez-Velamazán,[a, c] Javier Luzón,[b,c] Oriol Vallcorba,[d] Virginie Simonet,[e] Claire V. Colin,[e] and Juan Rodríguez-Carvajal.[a]

Abstract: The characterization of the crystal structure, phase transitions, magnetic structure and dielectric properties has been carried out on $[CH_3NH_3][Co(COOH)_3]$ (**1**) perovskite-like metal-organic compound through variable-temperature single-crystal and powder neutron and X-ray diffraction and relative permittivity measurements. The paraelectric to antiferroelectric-like phase transition observed at *ca.* 90 K is triggered by a structural phase transition; the structural studies show a change from *Pnma* space group at RT (**1A**) to $P2_1/n$ space group at low temperature (**1B**). This phase transition involves the occurrence of small distortions in the framework and counterions. Neutron diffraction studies have shown a magnetic order showing spontaneous magnetization below 15 K, due to the occurrence of a non-collinear antiferromagnetic structure with a weak ferromagnetic component, mainly due to the single-ion anisotropy of the Co(II) ions.

Introduction

Magnetic metal-organic frameworks have attracted intense interest in last years, not only from the fundamental point of view, but also from the possibility of development of new functional materials.[1] This previous interest has been increased considerably in recent years due to the combination within the same compound of two different ferroic-orders. This new generation of materials is called multiferroic metal-organic frameworks.[2] In particular, the coexistence of electric order in the same phase in which the long-range magnetic order occurs, although at substantially lower temperatures, is an exciting starting point for the design of new devices based on these new materials.[3]

Many of the multiferroic compounds are pure inorganic compounds belonging to the perovskite group. When electric and magnetic orders interact weakly with each other, these compounds are called proper-multiferroic materials of *Type I*.[4] In metal-organic multiferroics, the multiferroic behaviour is achieved combining an anionic metal-organic framework, responsible of the long-range magnetic order, with a counter ion located in the cavities of the framework. The adequate combination of these two elements could produce a compound with an order/disorder phase transition, frequently involving the hydrogen bond network,[2i,5] resulting in an electric order.

The survey of formate-based complexes is an interesting approach since they generally present perovskite-like structures, like most of the purely inorganic multiferroic materials. These structures combine a condensed metal network with a remarkable structural flexibility, and generally present a magnetic ordering due to the ability of the well-known formate ligand to mediate ferro- or antiferromagnetic coupling between metal ions depending on the coordination modes of the ligand (*syn-syn*, *anti-anti*, *syn-anti* or monoatomic coordination modes). The formate compounds have predilection for a $4^{12}\cdot6^3$-**cpu** topology, where the formate group acts as bis-monodentate in *anti-anti* coordination mode. This coordination gives rise to structures with medium size cavities where an adequate guest molecule can be located in order to promote electric order, in contrast with the well-known Prussian-blue analogues that present a compact NaCl-framework.[6] The maximum size of the counterions to keep the $4^{12}\cdot6^3$-**cpu** perovskite-like topology is of three non-hydrogen atoms, except for the ring-type counterions, like azetidinium and imidazolium. For bigger counterions, the inner chemical pressure precludes the formation of this topology. It deserves to be noted that slight changes in the weak interaction network between the host framework and the guest molecules promote remarkable changes in the physical properties, and therefore they are excellent candidates to be multiferroic materials.[7]

Among the first row transition metal ions containing unpaired electrons, the magnetochemistry of cobalt(II) systems is interesting due to their high anisotropy and d^7 electronic configuration, with occurrence of non-negligible spin-orbit coupling in the ground state. Thus, experimental and theoretical studies have been carried out by different groups in order to understand the magnetic properties of these systems.[8]

---

[a] L. Mazzuca, Dr. L. Canadillas-Delgado, Dr. O. Fabelo, Dr. J.A. Rodríguez-Velamazán and Prof. J. Rodríguez-Carvajal
Diffraction Group
Institut Laue Langevin
71 Avenue des Martyrs, CS 20156, 38042 Grenoble Cedex 9, France.
E-mail: lcd@ill.fr and fabel@ill.fr

[b] Dr. L. Canadillas-Delgado and Dr. J. Luzón
Centro Universitario de la Defensa de Zaragoza
Ctra Huesca s/n, Zaragoza 50090, Spain.

[c] Dr. J.A. Rodríguez-Velamazán and Dr. J. Luzón
Instituto de Ciencia de Materiales de Aragón, CSIC-Universidad de Zaragoza
C/ Pedro Cerbuna 12, E-50009, Zaragoza, Spain.

[d] Dr. O. Vallcorba
Alba Synchrotron
Cerdanyola del Vallès, Spain.

[e] Dr. V. Simonet and Dr. C. V. Colin
Institut Néel
CNRS and UJF BP 166, 38042 Grenoble Cedex 9, France.

Supporting information for this article is given via a link at the end of the document.

10.1002/chem.201703140

In the present work we investigate the structural, magnetic and dielectric properties of $[CH_3NH_3][Co(COOH)_3]$ (**1**) perovskite-like metal-organic compound.[9] The magnetic properties of this compound, based on magnetometry measurements, have been recently studied.[10] Magnetic measurements show that this material presents antiferromagnetic interactions with a weak ferromagnetic signal below 15.9 K, which the authors attribute to a spin canting as a consequence of Dzyaloshinskii-Moriya interactions among the Co(II) ions. Moreover, under high external magnetic field, this compound presents induced electric polarization showing magneto-electric behaviour.

As far as we know, the magnetic structure and the electric behaviour at zero magnetic field of this compound have not been studied before. These analyses are crucial for understanding the magnetic and electric behaviour giving rise to the previously reported magnetoelectric effect. This work is devoted to these studies through variable-temperature neutron and X-ray synchrotron diffraction and dielectric constant in the form of relative permittivity measurements. The analyses reveal a structural phase transition between 130 K and 50 K correlated with antiferroelectric-like order coexisting with magnetic order below 15 K.

Results and Discussion

Crystal Structure

The crystallographic studies at T = 300, 135 K and 45 K reveal a space group change from *Pnma* (high temperature (**1A**)) to $P2_1/n$ (low temperature (**1B**)). The resolution at low temperature can be done in the $P2_1/c$ standard group with unit cell dimensions of $a = 8.175(5)$, $b = 8.269(5)$, $c = 14.465(5)$ Å, $\beta = 126.270(5)$º (basis change from *Pnma* space group defined by –**c**, -**a**, **b**+**c**; 0, 1/2, 1/2). However, for the sake of clarity in the comparison of the crystallographic structures we will keep the $P2_1/n$ non-standard space group with $\beta = 91.89$º. This phase transition between *Pnma* and $P2_1/n$ non-standard group implies an overall permutation of the three crystallographic axis in the sense $a^{RT}=-b^{LT}$, $b^{RT}=-c^{LT}$ and $c^{RT}=a^{LT}$, together with a change on the β angle of 1.89º, keeping almost invariant its cell volume.

The existence of a group-subgroup relation between the orthorhombic *Pnma* and the monoclinic $P2_1/n$ space groups suggests that the observed phase transition may be of second order kind (continuous). However the coexistence of phases in the powder samples at low temperature (see below), points to a weak first-order character. This behaviour is not common for formate complexes presenting an order-disorder phase transition.[11] Although the crystal structure of complex **1A** has been described in previous papers,[9 -10] the structural phase transition has not been reported before. Both structures can be depicted as a 3D anionic $[Co(HCOO)_3]^-$ framework with a $4^{12}6^3$-**cpu** perovskite-like topology (in Schläfli notation). In order to achieve the electroneutrality, the framework cavities are filled with methylammonium cations $[CH_3NH_3]^+$. The perovskite structures are described as ABX_3 three-dimensional nets, where the A and B sites are occupied by two different cations and the X_3 positions are occupied by anions, which act as bridges between the B sites. The highest symmetry observed for pure inorganic perovskites is cubic, where the B cations are six-fold coordinated, forming regular octahedra, which are connected among them producing a final 3D network with cavities where the A elements are located. These perovskite structures can be related with our network being the $[NH_3CH_3]^+$ cation, the Co(II) atoms and the formate ligand, the A, B and X_3 sites, respectively. In our case, the cavity filled by the $[NH_3CH_3]^+$ cation (A site) within the 3-dimensional framework is about 204-208 Å^3, per unit cell at RT, and 190-191 Å^3 at 45K, where the neutron measurements give the smaller values compared with the X-rays, due to the more realistic determination of the light atoms ellipsoids.

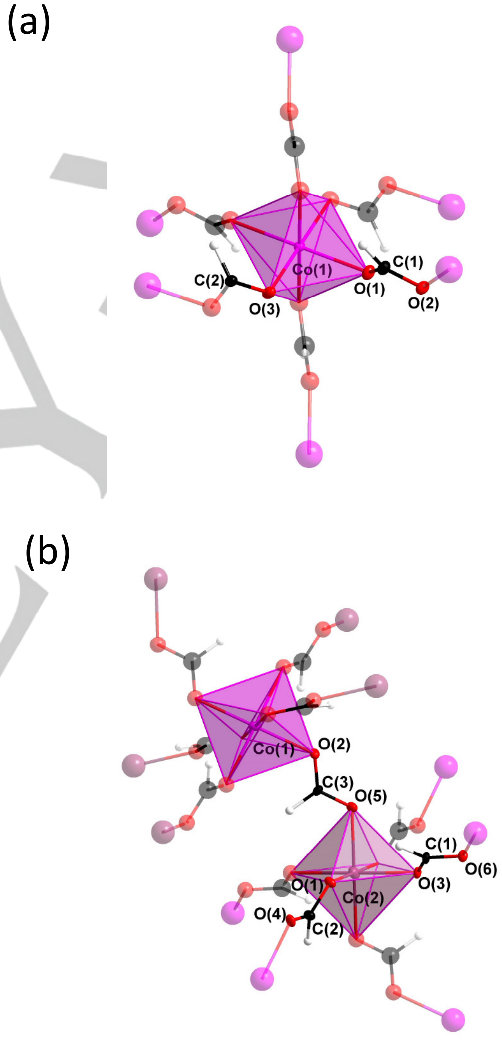

Figure 1. View of a fragment of the structure of **1A** (a) and **1B** (b), together with the atom numbering, obtained from the single crystal neutron refinement at 135 and 45 K, respectively. Octahedral Co(1) atom in **1A** complex (a) has been represented in pink while the Co(1) and Co(2) atoms in **1B** (b), have been represented in pink and purple, respectively. The oxygen, carbon and hydrogen atoms have been represented in red, black and light-gray, respectively. The ORTEP representation (50% ellipsoid probability) has been used to denote the asymmetric unit. The transparent mode was used to represent the atoms generated by symmetry operations. The methylammonium counter ions have been omitted for the sake of clarity.

Table 1. Selected bond lengths (Å) and angles (º) of compounds **1A** and **1B**.

RT		**1A**	Neutrons	RT		**1A**	X-rays
Co(1)-O(1)	2.0945(7)	Co(1)-O(1a^1)	2.0945(7)	Co(1)-O(1)	2.0932(6)	Co(1)-O(1a^1)	2.0932(6)
Co(1)-O(2b^1)	2.1169(7)	Co(1)-O(2c^1)	2.1169(7)	Co(1)-O(2b^1)	2.1191(6)	Co(1)-O(2c^1)	2.1191(6)
Co(1)-O(3)	2.1045(7)	Co(1)-O(3a^1)	2.1045(7)	Co(1)-O(3)	2.1054(8)	Co(1)-O(3a^1)	2.1054(8)
Co(1)-O(1)-C(1)	122.24(5)	Co(1)···Co(1b^1)	5.8348(1)	Co(1)-O(1)-C(1)	122.46(6)	Co(1)···Co(1b^1)	5.8411(10)
Co(1)-O(2)-C(1b^1)	120.84(5)	Co(1)···Co(1c^1)	5.8348(1)	Co(1)-O(2)-C(1b^1)	120.72(6)	Co(1)···Co(1c^1)	5.8411(10)
Co(1)-O(3)-C(2)	122.11(4)	Co(1)···Co(1d^1)	5.8590(2)	Co(1)-O(3)-C(2)	122.21(6)	Co(1)···Co(1d^1)	5.8608(2)
135K				**1A**			**Neutrons**
Co(1)-O(1)	2.0892(5)	Co(1)-O(1a^1)	2.0892(5)	Co(1)-O(1)-C(1)	121.45(3)	Co(1)···Co(1b^1)	5.8115(1)
Co(1)-O(2b^1)	2.1135(4)	Co(1)-O(2c^1)	2.1135(4)	Co(1)-O(2)-C(1b^1)	120.05(3)	Co(1)···Co(1c^1)	5.8115(1)
Co(1)-O(3)	2.1002(5)	Co(1)-O(3a^1)	2.1002(5)	Co(1)-O(3)-C(2)	121.40(3)	Co(1)···Co(1d^1)	5.8368(1)
45K		**1B**	**Neutrons**	**45K**		**1B**	**X-rays**
Co(1)-O(2)	2.090(3)	Co(2)-O(1)	2.083(3)	Co(1)-O(2)	2.1003(16)	Co(2)-O(1)	2.0813(16)
Co(1)- O(2a^2)	2.090(3)	Co(2)-O(1d^2)	2.083(3)	Co(1)- O(2a^2)	2.1003(16)	Co(2)-O(1d^2)	2.0813(16)
Co(1)- O(6b^2)	2.096(3)	Co(2)-O(3)	2.102(3)	Co(1)- O(6b^2)	2.0967(15)	Co(2)-O(3)	2.1048(16)
Co(1)- O(6c^2)	2.096(3)	Co(2)-O(3d^2)	2.102(3)	Co(1)- O(6c^2)	2.0967(15)	Co(2)-O(3d^2)	2.1048(16)
Co(1)- O(4e^2)	2.096(3)	Co(2)-O(5)	2.121(3)	Co(1)- O(4e^2)	2.1075(17)	Co(2)-O(5)	2.1207(16)
Co(1)- O(4f^2)	2.096(3)	Co(2)-O(5d^2)	2.121(3)	Co(1)- O(4f^2)	2.1075(17)	Co(2)-O(5d^2)	2.1207(16)
Co(1)-O(4e^2)-C(2e^2)	120.02(24)	Co(2)-O(5)-C(3)	120.04(24)	Co(1)-O(4e^2)-C(2e^2)	120.45(14)	Co(2)-O(5)-C(3)	119.52(15)
Co(1)-O(2)-C(3)	120.92(23)	Co(2)-O(3)-C(1)	120.26(18)	Co(1)-O(2)-C(3)	120.53(15)	Co(2)-O(3)-C(1)	120.35(16)
Co(1)-O(6b^2)-C(1b^2)	122.27(19)	Co(2)-O(1)-C(2)	121.44(22)	Co(1)-O(6f^2)-C(1f^2)	122.09(15)	Co(2)-O(1)-C(2)	121.62(14)
Co(1)···Co(2)	5.8022(1)	Co(1)···Co(2c^2)	5.8292(2)	Co(1)···Co(2)	5.8146(2)	Co(1)···Co(2c^2)	5.8365(3)
Co(1)···Co(2f^2)	5.8022(1)			Co(1)···Co(2f^2)	5.8146(2)		

Symmetry code **1A**: *a*^{1}: *-x*+1, *-y*, *-z; b*^{1}: *x*-1/2, *y*, *-z*+1/2; *c*^{1}: *x*-3/2, *-y*, *z*-1/2.
Symmetry code **1B**: *a*^{2}: *-x*, *-y*+1, *-z; b*^{2}: *x*-1/2, *-y*+1/2, *z*-1/2; *c*^{2}: *-x*+1/2, *y*+1/2, *-z*+1/2*; d*^{2}: *-x*+1, *-y*, *-z; e*^{2}: *-x*, *-y*, *-z; f*^{2}: *x*, *y*+1, *z.*

There is one crystallographically independent Co(II) ion in **1A**, located at an inversion centre. The Co(II) ion is six-coordinated in almost ideal CoO_6 octahedral surroundings, with values of the twisting parameter (ϕ) and compression ratio (*s/h*)*,* derived from neutron data, of about 60° and 1.3, respectively at RT, (ϕ = 60° and *s/h* = 1.22 for an ideal octahedron).[12] At 135 K these values remain almost equal. The equatorial plane of Co(1) is built up by O(1), O(3), O(1a^1) and O(3a^1) [*a*^{1}: *-x*+1, *-y*, *-z*] while the axial positions are filled by O(2b^1) and O(2c^1) [*b*^{1}: *x*-1/2, *y*, *-z*+1/2; *c*^{1}: *x*-3/2, *-y*, *z*-1/2] carboxylate-oxygen atoms (see Figure 1). In the low temperature phase, there are two crystallographically independent cobalt(II) ions [Co(1) and Co(2)], both located in inversion centres. Each Co(1) is surrounded by six Co(2), and every Co(2) is surrounded by six Co(1) ions, building in both cases an octahedral arrangement (see Figure 1). Their coordination polyhedra, are built by six oxygen atoms, forming an almost ideal octahedral environment, with geometric values ϕ of about 59° and 61° and *s/h* 1.31 and 1.32, for Co(1) and Co(2), respectively, obtained from neutron measurements.[12] The equatorial plane is built up by O(2), O(2a^2), O(6b^2) and O(6c^2) [*a*^{2}: *-x*, *-y*+1, *-z; b*^{2}: *x*-1/2, *-y*+1/2, *z*-1/2; *c*^{2}: *-x*+1/2, *y*+1/2, *-z*+1/2] for Co(1) and O(1), O(3), O(1d^2) and O(3d^2) [*d*^{2}: *-x*+1, *-y*, *-z*] for Co(2), while the axial positions are filled by for O(4e^2) and O(4f^2) for Co(1) and O(5) and O(5d^2) for Co(2) [*e*^{2}: *-x*, *-y*, *-z; f*^{2}: *x*, *y*+1, *z*]. The cobalt(II) ions in **1A-1B** are connected through formate ligands in *anti-anti κOO'* coordination mode along the [1 0 1], [0 1 0] and [1 0 -1] directions for **1A** and along the [-1 1 0], [1 1 0] and [0 0 1] directions for **1B** (see Figure 2). The values of the Co-O-C angle for the carboxylate bridge are in the range from 120.84(5)° to 122.11(4)° for **1A** at RT, and from 120.02(24)° to 122.27(19)° for **1B** at 45K, while the Co···Co distances vary from 5.8348(1) to 5.8590(2) Å for **1A** and from 5.8022(1) to 5.8292(1) Å for **1B** (see Table 1).

The phase transition involves the occurrence of a slight reorientation of the methylammonium ions into the cavities as well as a small distortion of the framework, in a sort of displacive transition (see Figure 2d-e). In the **1A** structure, a mirror plane through the nitrogen and carbon atoms parallel to the *ac*-plane traverses the methylammonium molecule. At RT, the hydrogens connected to the carbon atoms are disordered in two positions [H(3A), H(3B) and H(3C) with torsion angle H(3A)-C(3)-N(1)-

10.1002/chem.201703140

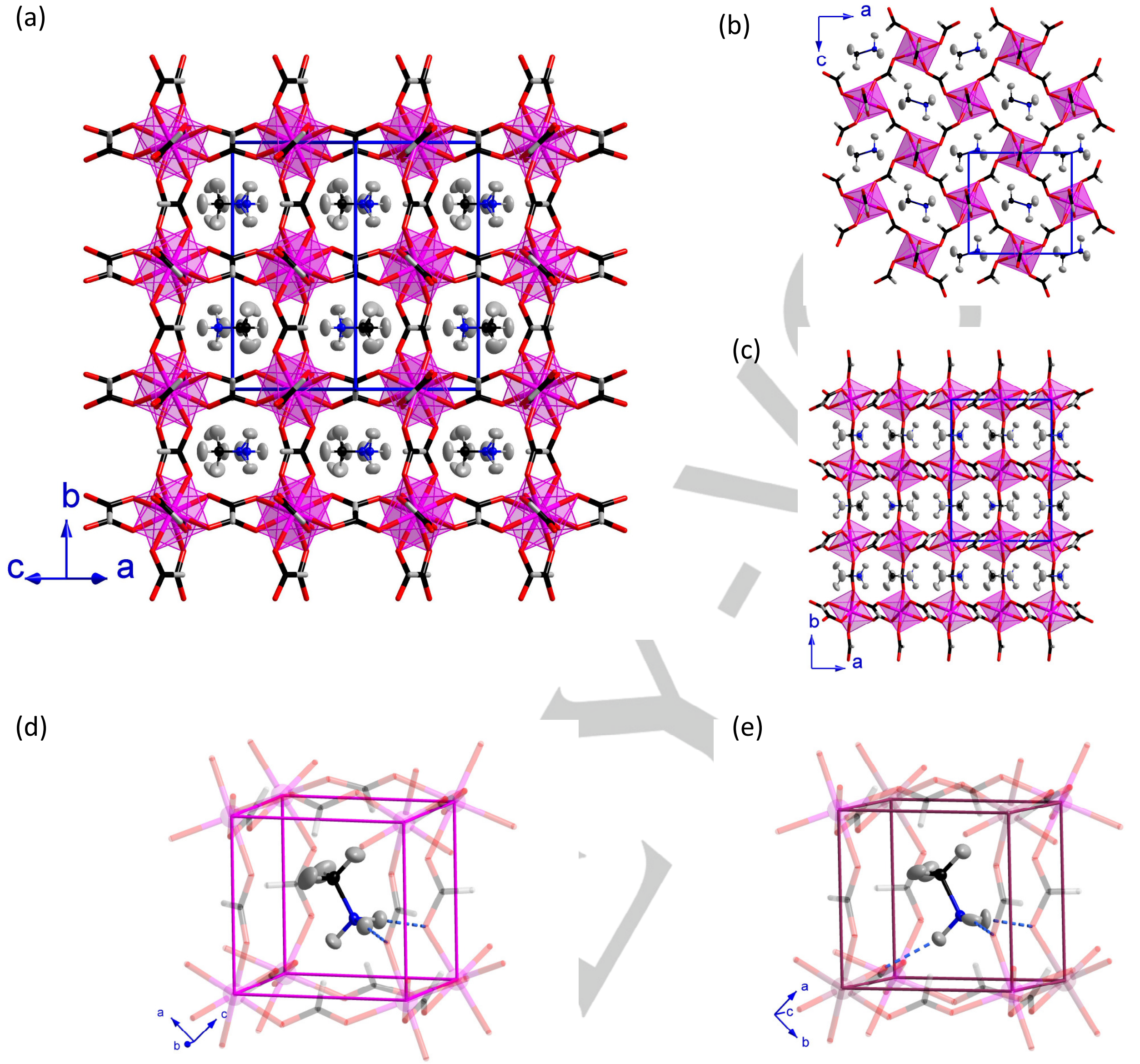

Figure 2. (a) View along the [1, 0, 1] direction of a fragment of the structure of **1A**, obtained from the single crystal neutron diffraction at 45 K. (b) and (c) correspond to views along the *b*- and *c*-axis, respectively. (d) and (e) figures show a detail of the metal-organic cage, where the methylammonium molecule, is located at 135 and 45 K, respectively. The nitrogen atoms of the methylammonium counterions have been represented in blue. The rest of the atoms follow the same color codes as in previous figure. The H-bond network of the methylammonium molecules with the framework has been represented as dashed blue lines. The pink (d) and purple (e) bonds are only a guide to the eye.

H(2Nd^1) of 51.8(12)°, and H(3Ad^1), H(3Cd^1) and H(3Bd^1) with torsion angle H(3Ad^1)-C(3)-N(1)-H(2Nd^1) of 68.2(12)°]. This disorder can be indicative of a rotation around the C-N axis. When the system reaches 135 K, the entire molecule sits in a single crystallographic position where the hydrogen atoms bonded to the carbon atom are H(3A), H(3B) and H(3Bd^1) with torsion angle H(3A)-C(3)-N(1)-H(2Nd^1) of 60.01(15)°, indicating that the possible rotation of the hydrogen atoms from the CH_3- unit disappears, although the ellipsoids of these hydrogen atoms remain bigger than those of the NH_3- unit (see Figure 3). Once the low temperature phase is achieved (**1B**), the mirror plane is lost, and then there are six crystallographically independent hydrogen atoms [H(6), H(9) and H(5) in the CH_3- unit and H(1), H(2) and H(8) in the NH_3-]. All these variations imply slightly changes in the distances of the hydrogen bond network where the methylammonium molecule is involved (see Table 2 and Figure 3). Regarding the host framework, there are some slight changes in the Co(II) ion octahedral environment. Mainly all Co-O distances of the octahedral environments become shorter at low temperature, except the apical distance which changes from

10.1002/chem.201703140

2.1135(4) Å at 135 K [Co(1)-O(2b^1)] to 2.1212(1) Å at 45 K [Co(2)-O(5)]. Furthermore, the apical distances of the Co(1) ion in compound **1B** [Co(1)-O(6b^2) = 2.096(3) Å] is shortened, reaching almost the same value as one of the equatorial distances [Co(1)-O(4e^2) = 2.096(3) Å]. The distances in the formate ligands remain almost identical being in the range from 1.2467(1) Å to 1.2628(1) Å at 135 K and in the range from 1.246(3) Å to 1.268(4) Å at 45 K. However the angles in the ligands become slightly larger from 123.485(1)-124.312(1) at 135 K to 123.7(2)-124.7(3) at 45 K.

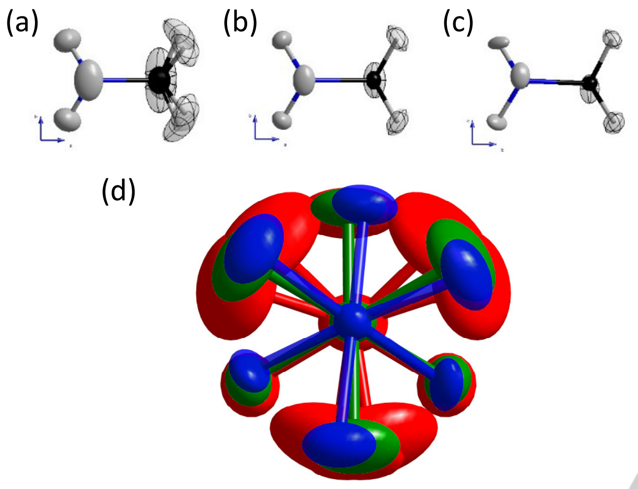

Figure 3. (a-c) Detailed view of the methylammonium molecule at RT, 135 and 45 K obtained from the single crystal neutron diffraction measurements. The atoms, including the hydrogens, have been represented in ellipsoid mode with a 30% of probability. The hydrogen atoms from the CH_3 groups have been represented in transparent mode together with a principal ellipses. (d) View along the C-N bond of the methylammonium molecule at RT, 135 and 45 K, red, green and blue, respectively.

Table 2. Possible hydrogen bonds of compounds **1A** and **1B** determined from neutron diffraction.

1A at RT	Donor···Acceptor (Å)	H···Acceptor (Å)	Donor-H···Acceptor (º)
N(1)-H(2N)···O(2f^1)	2.8834(9)	1.851(2)	173.66(19)
N(1)-H(2Nd^1)···O(2e^1)	2.8834(9)	1.851(2)	173.66(19)

1A at 135 K	Donor···Acceptor (Å)	H···Acceptor (Å)	Donor-H···Acceptor (º)
N(1)-H(2N)···O(2f^1)	2.8583(5)	1.8202(13)	173.86(10)
N(1)-H(2Nd^1)···O(2e^1)	2.8583(5)	1.8202(13)	173.86(10)

1B at 45 K	Donor···Acceptor (Å)	H···Acceptor (Å)	Donor-H···Acceptor (º)
N(1)-H(2)···O(5)	2.845(3)	1.828(7)	174.9(5)
N(1)-H(8)···O(4c^2)	2.876(3)	1.834(7)	172.3(5)
N(1)-H(1)···O(3g^2)	2.955(4)	1.991(7)	153.2(5)

Symmetry code **1A**: d^1: x, $-y+1/2$, z; e^1: $-x+3/2$, $-y$, $z-1/2$; f^1: $-x+3/2$, $y+1/2$, $z-1/2$
Symmetry code **1B**: c^2: $-x+1/2$, $y+1/2$, $-z+1/2$; g^2: $-x+3/2$, $y+1/2$, $-z+1/2$

Due to the small distortion of the framework together with the reorientation of the methylammonium counter ions, the number of hydrogen bonds at LT is larger than those observed at RT, being the Donor···Acceptor distances 2.8834(9) at RT and in the range of 2.845(3) and 2.955(4) Å at 45 K. This contributes to the anchoring of the methylammonium counterion in the cavities as well as to the global crystal structure stabilization (see Figure 2). All these changes in the structure promote that the evolution in temperature of the unit cell parameters does not follow an isotropic diminution with the decreasing of temperature. Moreover, the *b*-axis increases slightly upon cooling.

X-ray Powder Diffraction Measurements

Synchrotron X-ray powder diffractograms have been collected at RT and at 45 K, above and below the structural phase transition, respectively. At RT the model in *Pnma* space group fits well the experimental data (see Figure 4a), however, at low temperature the measurements show more reflections than expected for the monoclinic phase (see the inset in Figure 4b). Moreover, some of the narrow reflections observed at RT become broad at 45 K. This suggest a non-negligible occurrence of strains after the phase transition.

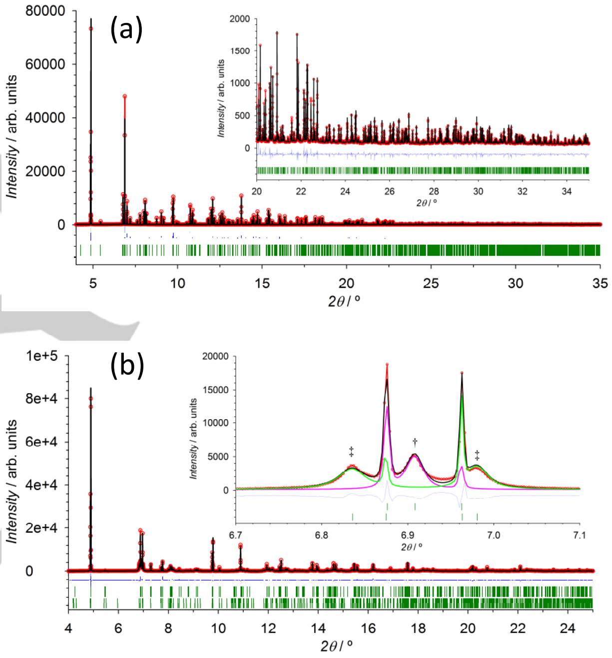

Figure 4. (a) Experimental (open red circles) synchrotron X-ray powder diffraction data and calculated Rietveld refinement (black solid line) pattern for compound **1** at RT (data collected with λ= 0.4948 Å). The difference between observed and calculated patterns has been represented as a blue line. The vertical green marks represent the position of the Bragg reflections. The inset shows a zoom of the high-angle region. Refined cell parameters $a = 8.392869(8)$, $b = 11.707005(8)$ and $c = 8.104255(7)$ Å, $\alpha = \beta = \gamma = 90.0°$. The data refinement gives, $R_B = 9.40$ % and $R_F = 5.55$ %, as agreement factors. (b) Le Bail fit of the same sample collected at 45 K. The code of colours has the same meaning that in (a). The upper raw of vertical green marks represent the position of the Bragg reflections for the orthorhombic phase. While the lower raw shows the position corresponding to the monoclinic phase, with refined cell parameters of $a = 8.26226(3)$, $b = 11.6471(2)$ and $c = 8.15991(3)$ Å, $\alpha = \beta = \gamma = 90.0°$ and $a = 8.16148(2)$, $b = 8.26332(1)$ and $c = 11.65342(7)$ Å, $\beta = 91.676(1)°$ for the orthorhombic and monoclinic phase, respectively. The inset show in detail the contribution of each phase. The intensity corresponding to the orthorhombic and monoclinic phases is represented by pink and green solid lines, respectively. It should be noted that the orthorhombic (1 2 1) reflection, marked with † symbol is split into the (-1 1 2) and (1 1 2) reflections in the monoclinic phase, marked with ‡ symbols in the figure.

10.1002/chem.201703140

The low temperature data were analysed using a Le Bail fit. The indexing of the low temperature pattern using a single phase was unsuccessful, and the best refinement model was obtained with a mixture between **1A** and **1B** phases. It deserves to be noted that this mixture of two phases was not observed in neither the single crystal X-ray nor single crystal neutron diffraction. In order to take into account anisotropic broadening, a quartic form in (*h k l*) for the strain was used during the fit (see Figure 4b). Figure S1 in the supplementary information shows the comparison of the micro-strain results between high- and low-temperature phases, suggesting an increase of strain after the phase transition. The occurrence of strain in the sample can be consequence of the atomic displacement giving rise to the monoclinic twin-domains observed in the single crystal data (see details in the Experimental Section). Two different samples were measured at low temperature (ca. 45K, see Figure S2 in the supplementary information), and although both are similar, the differences suggest a temperature dependence of the strain pattern as well as in the ratio between the orthorhombic and monoclinic phases. Due to the large overlapping between the orthorhombic and monoclinic phases (related by a group-subgroup relation) together with the broadening of some reflections, the Rietveld refinement including both phases is not stable and therefore we limit our analysis of powder sample to the described Le Bail fit.

Heat Capacity

The heat capacity data reveal a λ-shaped peak at 15 K, corresponding to the magnetic ordering. At higher temperature the heat capacity has been explored, but there is no signal that could be associated with the structural phase transition. This absence of signal can be attributed to a low energetic phase transition, which can be present in an extended range of temperatures.

The low temperature peak in the heat capacity suggests the compound has a 2D or 3D magnetic dimensionality.[13] In order to study the entropy related with the magnetic transition, we carried out a background correction by subtracting the phonon contribution (AT^3 term) (see Figure S3 in the supplementary information). The value of A was fixed to give no magnetic contribution well above the magnetic transition (above 20 K). The magnetic entropy was derived by integration of the C_p/T versus T plot up to 20 K, once the AT^3 contribution subtracted. The value of the entropy approaches 5.86 J mol^{-1} K^{-1} (per cobalt atom), half of the expected 11.5 J mol^{-1} K^{-1} for the magnetic entropy $R \cdot \ln(2s + 1)$ if $s = 3/2$. Nevertheless, cobalt is known to have $s_{eff} = 1/2$ at low temperatures,[14] thus the value of 5.86 J mol^{-1} K^{-1} is in good agreement with the one expected one for $s = 1/2$ (5.76 Jmol^{-1}K^{-1}).

Dielectric measurements.

The dielectric constant in the form of relative permittivity (ε_r) is shown in Figure 5a. The relative permittivity decreases linearly from 8.86 at 250 K to 8.54 at 103 K. At this temperature, a clear change in the slope is observed as a drop from 8.54 to 8.47 at 80 K. This anomaly is continuous, which is compatible with second-order or with sluggish first order phase transition. Below this event, the permittivity value decreases in a linear way to reach a value of 8.35 at 6 K. It deserves to be noted that at T_N the relative permittivity remains almost constant, discarding the occurrence of a magneto-electric effect. The shape of the signal suggests the occurrence of an antiferroelectric-like phase transition at *ca.* 103 K. The continuous variation in the slope of ε_r *vs* T as well as the smooth jump at the phase transition temperature, suggest that the structural phase transition occurs in a large temperature range. Moreover, the powder diffraction data show a non-negligible mixture of phases at low temperature that depends of the cooling/warming process (see Figure S2 in the supplementary information). This can be at the origin of the slight difference observed in the permittivity between the cooling and the warming curves.

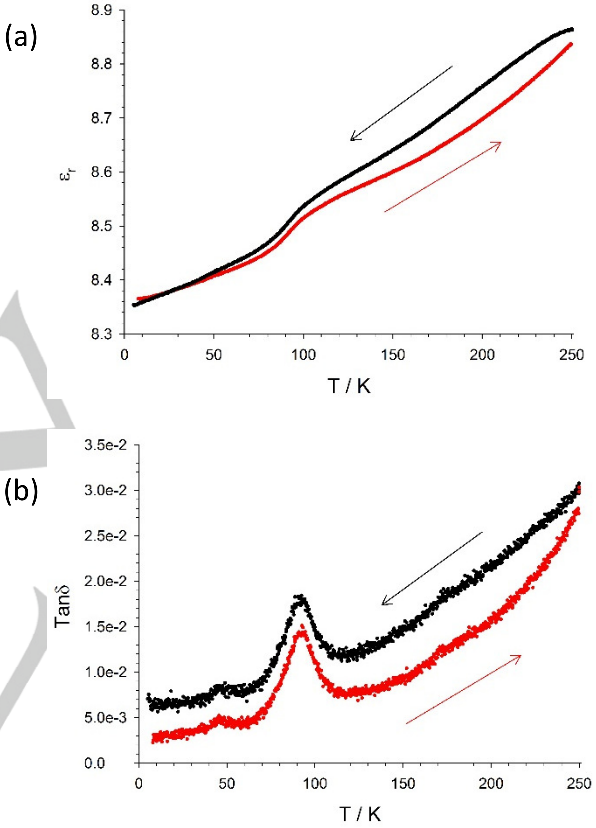

Figure 5. (a) Relative permittivity as a function of temperature (red curve on cooling and black curve on warming). The measurement was done on a pellet sample at 10 kHz, using an amplitude of 1V. (b) Temperature dependence of the dielectric loss of $[CH_3NH_3][Co(COOH)_3]$ compound, at zero magnetic field. See further details in the experimental section.

In Figure 5b we show the dielectric loss given as loss tangent of compound **1** as a function of temperature. The dissipation factor of compound **1** estimated at 9 K is about $2.8 \cdot 10^{-3}$, a value which increases upon warming to $4.8 \cdot 10^{-3}$ at 45 K. After this point, the resistivity decreases to $4.2 \cdot 10^{-3}$ at 58 K. This valley in the resistivity curve is hardly perceptible in the permittivity measurement, and related with the transition of only part of the sample from **1A** to **1B** phases upon cooling, as the powder diffraction measurements show. Warming up, the resistivity increase abruptly until $1.5 \cdot 10^{-2}$ at 92 K and decrease again to

10.1002/chem.201703140

$7.6\cdot10^{-3}$ at 113 K. These variations in the dielectric loss appear within a broad range of temperatures, which can be correlated with the freezing of the methylammonium libration (mainly the methyl-groups), and/or with the slight structural variations in the framework. This anomaly corresponds to the change in the slope observed in the relative permittivity. After 113 K the resistivity increases smoothly up to $3.0\cdot10^{-2}$ at 250 K.

Upon cooling, changes in the dissipation factor curve appear at the same temperatures as warming up. The discrepancy between both curves can come from defects in the pellet due to the thermal cycles or because of a variation in the orthorhombic/monoclinic phase ratio during cooling.

From these results we conclude that the $[CH_3NH_3][Co(COOH)_3]$ compound presents a transition from paraelectric to antiferroelectric-like behaviour in the range from 120 K to 45 K, where the dissipation factor of the sample undergoes variations because of the change of the space groups (both non-polar). The broad shape of these fluctuations agrees with the lack of a peak in the heat capacity measurements, which suggests a slow reorganization of the structure in a broad range of temperatures. This scenario is compatible with the continuous change of intensity in the neutron powder diffraction data as function of the decreasing temperatures (see Neutron Powder Diffraction section).

Neutron Powder Diffraction Analysis

Neutron powder thermodiffractograms in the 20-300 K and 2-20 K ranges have been collected in order to explore the structural and magnetic phase transitions, respectively, in the D1B high flux diffractometer at ILL (see Neutron Powder Diffraction Measurements section for details). The 20-300 K neutron thermodiffractogram shows a progressive increase of intensity on some Bragg reflections with small differences in the unit cell until ca. 80 K (see Figure 6a). At this temperature, there is a clear change in the reflections, which agrees with a structural phase transition. Below this temperature, a mixture of orthorhombic and monoclinic phases is needed to fit properly the data, which is compatible with the previous powder X-ray data. At lower temperatures, the thermodiffractogram shows an increase of intensity of some Bragg reflections below 15 K, corresponding with the occurrence of a long-range magnetic ordering, which is in agreement with the magnetic susceptibility measurements. The appearance on the top of the Bragg reflections of the observed magnetic contribution is indicative of a **k** = (0, 0, 0), magnetic propagation vector (see Figure 6b).

The magnetometry measurements of **1** have been recently reported on single crystal and powder samples.[10] These measurements reveal a global antiferromagnetic behaviour with ferromagnetic component below 15.9 K. The single crystal analyses show that this ferromagnetic contribution accounts for 0.19 μ_B in the [0, 1, 0] direction (in the orthorhombic description). Moreover, in these measurements a negative magnetization appears below 7 K, which the authors assign to a remnant field in the magnet.

In order to determine the possible magnetic structures at zero applied magnetic field, a series of neutron diffraction measurements above and below the ordering temperature have been carried out. Due to the weak magnetic contribution, the overlap between nuclear reflections and the considerable background produced by the high number of hydrogen atoms in the sample, our data preclude the accurate determination of the nuclear and the magnetic structure at the same time. Alternatively, the nuclear contribution has been subtracted from the low temperature pattern at 2 K, using the nuclear intensity of the paramagnetic phase measured at 20 K. Both diffraction patterns were normalized to the same monitor to obtain the best difference pattern. This difference pattern isolates the magnetic contribution and therefore, a more accurate indexing of the magnetic reflections as well as an explanation of the magnetic structure can be undertaken (see Figure 7).

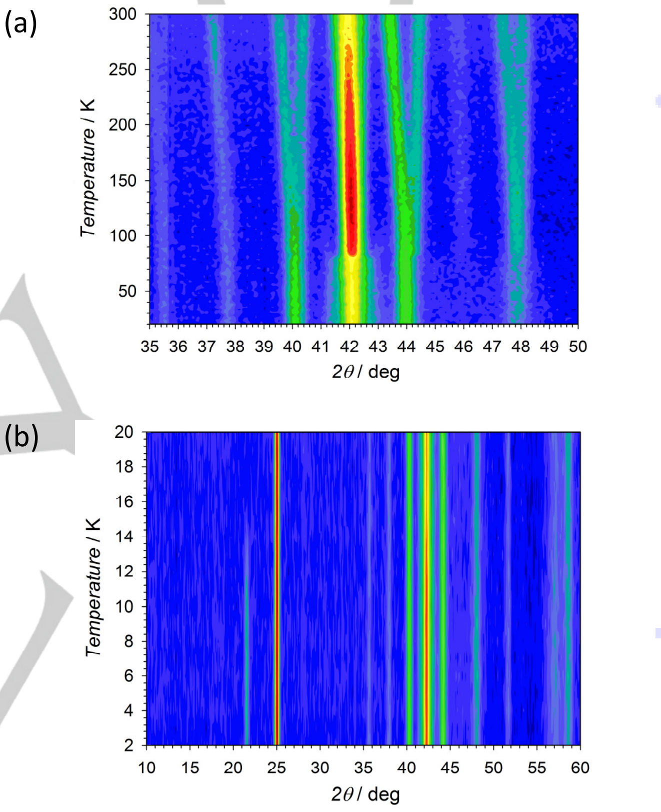

Figure 6. (a) Mesh plot, with the intensities repersented in logarithmic scale, of the thermodiffractogram collected at D1B in the temperature range of 20-300 K. The figure shows the changes of intensities of the nuclear reflections from RT to the phase transition temperature at ca. 80 K. Below this temperature the orthorhombic and monoclinic phase coexist (see main text). (b) Mesh plot of the thermodiffractogram in the temperature range of 2-20 K. The appearance of new reflections and the increase of intensity on the top of the nuclear reflections below 15 K, is in agreement with the reported T_N of this compound see ref. [10**Error! Bookmark not defined.**].

In contrast with the single crystal measurements, where at low temperature the crystal structure changes to a single $P2_1/n$ phase, the powder diffraction measurements show that at low temperature both phases **1A** and **1B** coexist. We will then consider both phases in the analysis of the magnetic structure. In order to accomplish the symmetry analyses, we have considered both phases separately.

Four irreducible one-dimensional representations of the group G_k, (Γ_1-Γ_4) and a simple set of basis vectors for each irreducible representation can be determined using the program BasIreps[15] for *Pnma* and $P2_1/n$ structures. The representational analysis provides the expression of the Fourier vector coefficients (in this case equivalent to magnetic moments) as linear combinations of basis functions. The basis vectors describe the possible magnetic structures.

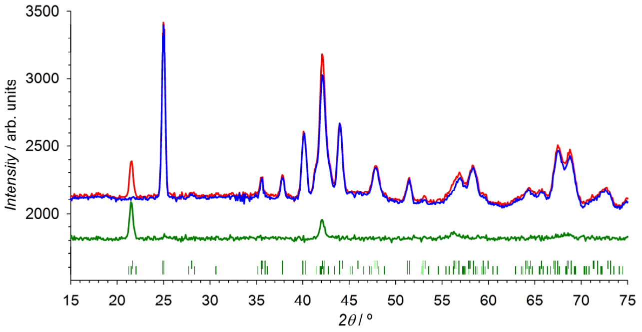

Figure 7. Neutron powder patterns of **1** collected at 2 K (blue) and 20 K (red) using the high flux D1B diffractometer. The difference diffraction pattern has been represented in green. The intensity of the calculated difference pattern has been shifted to an arbitrary value in order to achieve a similar background than those observed in the original patterns. The vertical lines represent the Bragg positions for compound **1A** (top) and **1B** (bottom).

Considering the *Pnma* space group (**1A**), the four irreducible representations are compatible with the Wyckoff position of the Co(II) atoms (4*b* Wyckoff positon) and the propagation vector **k** = (0, 0, 0). These four representations correspond to four magnetic groups; *Pnm'a', Pnma, Pn'm'a* and *Pn'ma'*, in Shubnikov notation and all them were tested to fit the difference pattern. The *Pnm'a'* magnetic model can be discarded since it is far from fitting properly the magnetic data. The *Pnma* model reproduces well the experimental data, but the obtained magnetic model agrees with a strictly antiferromagnetic structure, in contrast with the magnetometry measurements, which show a clear ferromagnetic contribution. *Pn'm'a* and *Pn'ma'* magnetic groups are also in agreement with the experimental data, and permit a ferromagnetic component (see Figure 8). The best fit of the *Pn'm'a* magnetic model to the neutron data provides an antiferromagnetic structure with a small ferromagnetic contribution along the *c*-axis (*c* = 8.1543(2) Å) of 0.44 μ_B per Co ion due to a spin canting. However, this model does not allow any contribution along the *b*-axis, being strictly antiferromagnetic in this direction, and therefore we can discard it.

The refined model on the *Pn'ma'* group presents a ferromagnetic contribution along the orthorhombic *b*-axis [*b* = 11.6735(2) Å]. Nevertheless, this contribution is about 0.68(12) μ_B per Co(II) ion, which is higher than the signal encountered along this axis in ref. [**Error! Bookmark not defined.**] (0.19 μ_B). However, the single crystal diffraction data at 45 K showed that once the sample achieves the phase transition it becomes a twinned crystal. Depending on the relation between the twin domains, the magnetic contribution can change. The twin-domains observed in the single crystal experiments (neutrons and X-ray) are related by a rotation of 180º with respect to the shortest axis (*a*-axis in the orthorhombic base), that is, perpendicular to the ferromagnetic component. As consequence of these twin-domains, the ferromagnetic contribution obtained from the single-crystal magnetometry measurements can be underestimated depending on the twin-domain balance. The obtained value for the Co(II) magnetic moment is 2.9(2) μ_B, which is reasonable for a high-spin divalent cobalt ion.

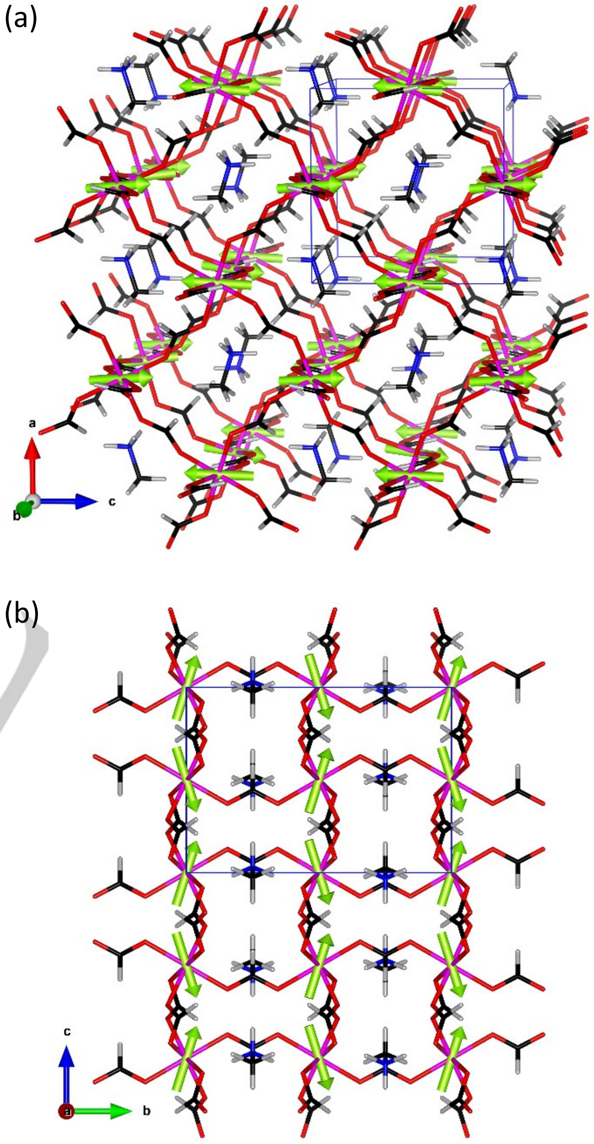

Figure 8. (a) Perspective view along the *b*-axis of the magnetic structure refined in the *Pn'ma'* Shubnikov space group. (b) Detail view along the *a*-axis. The crystal and magnetic unit cell [**k** = (0, 0, 0)], has been represented in blue and the magnetic moments in light green. The nuclear structure has been represented using the same code of colors than in the previous figures. The atoms follow the same color codes as in previous figures.

10.1002/chem.201703140

Regarding the monoclinic crystal structure (**1B**), the magnetic representation Γ_M for each magnetic site [Wyckoff position 2*b* for Co(1) and for 2*c* for Co(2)] can be decomposed as direct sum of two of the irreps, Γ_1 and Γ_3, by applying the great orthogonality theorem. Each irrep appears three-times for 2*b* and 2*c* sites.

$$\Gamma_M(2b) = 3\Gamma_1 \oplus 3\Gamma_3 \quad (1)$$

$$\Gamma_M(2c) = 3\Gamma_1 \oplus 3\Gamma_3 \quad (2)$$

There are two independent magnetic sites [Co(1) and Co(2)], so there are six degrees of freedom to refine these magnetic structures. The number of parameters can be reduced assuming the same magnetic moment for both magnetic sites. The Shubnikov groups corresponding to Γ_1 and Γ_3 are $P2_1/n$ and $P2'_1/n'$ [with (**a**, **b**, **a**+**c**; 0, 0, 0) transformation to the $P2'_1/c'$ standard magnetic space group], respectively. The $P2_1/n$ model gives a magnetic structure where the magnetic moments are almost antiferromagnetically coupled in all directions, which does not explain the ferromagnetic signal in the magnetometry measurements. Moreover, it is not able to fit properly the experimental data. The best fit of $P2'_1/n'$ model gives a magnetic structure that permits the occurrence of weak ferromagnetism (see Figure S4 in the supplementary information), as observed in the magnetometry measurements.

Due to the contribution of both phases in the low temperature pattern, with a ratio between orthorhombic and monoclinic phases of 56 and 44%, respectively (see Figure S5 in the supplementary information), a magnetic structure refinement have been carried out combining the two possible magnetic space groups. As the monoclinic distortion is not very large and in order to avoid overparametrization, in the initial refinements both magnetic structures were restrained to be the same. This constraint is supported by the observation of magnetic intensities only on top of the reflections coming from the orthorhombic space group. Therefore, some constraints were added to the monoclinic $P2'_1/n'$ magnetic space group to reproduce the magnetic structure of the orthorhombic *Pn'ma'* magnetic space group. Only in the last refinement, the monoclinic phase has been refined independently. Due to the low number of magnetic reflections, the *a*- and *b*-components of the two magnetic sites of the monoclinic phase have been constrained to be antiferromagnetically coupled, as was observed in the orthorhombic phase (*a*- and *c*-component in the orthorhombic space group). The refined magnetic moment of Co(1) and Co(2) are equal within the experimental error, with a value of 2.9(2) μ_B.

In summary, the neutron diffraction results at 2 K yield *Pn'ma'* and $P2'_1/n'$ magnetic models, which give rise to magnetic structures where the magnetic moments are antiferromagnetically coupled, with a small non-compensated component of the magnetic moment.

The obtained magnetic space groups have the spatial inversion as a symmetry operator and therefore they are not compatible with an electric polarization at zero-field induced by the spin arrangement. Consequently, the magneto-electric coupling at zero-field should not be significant. The previously observed magneto-electric coupling under applied magnetic field should be correlated with a different field-induced magnetic structure.

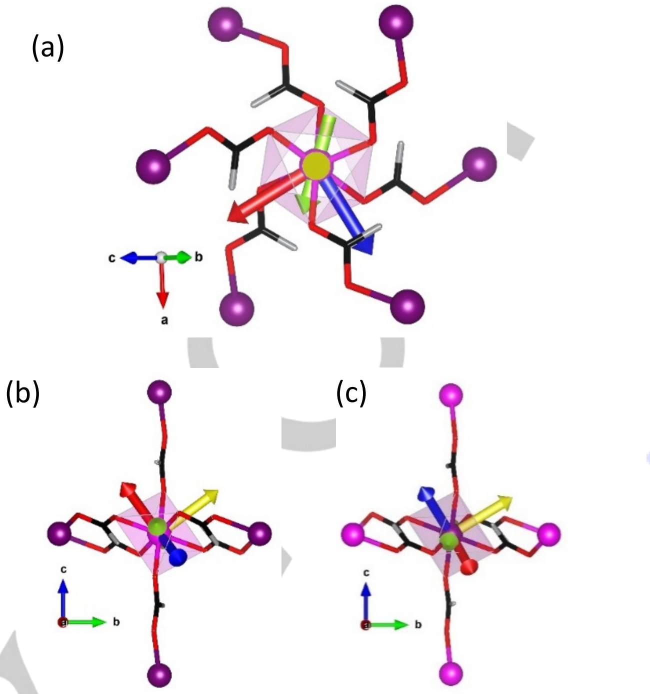

Figure 9. (a) View of the single-ion magnetic anisotropy axes seen along the pseudo S_6 axis of the distorted octahedral environment around the Co(1) ion. Hard axis (yellow), easy axis (red) and intermediate axis (blue). The refined magnetic moment has been represented in light green. (b-c) View of the superposition of the experimental model and the single-ion magnetic anisotropy axes for Co(1) and Co(2) ions along the crystallographic *a*-axis (in the $P2'_1/n'$ magnetic space group). Methylammonium molecules have not been included for the sake of clarity.

Discussion

In the title compound the strongest magnetic interactions must be those due to the Co(II)-formate-Co(II) super exchange pathways resulting in a 3-dimensional magnetic network. In such magnetic network, each Co(II) ion is coupled with other four Co(II) ions in the *ab*-plane, using the monoclinic description (or *ac*-plane in the orthorhombic space group), by two magnetic interactions J_1 and J_2, and with two other Co(II) ions along the *c* direction by a J_3 magnetic interaction (see Figure S6 in the supplementary information). These three magnetic interactions are expected to be of the same order of magnitude, due to their very similar magnetic pathway geometries, and antiferromagnetic in nature. Due to the slight distortion after the structural phase transition, this scenario is also valid for the orthorhombic space group. Since there is no frustration in the magnetic network, an antiferromagnetic collinear structure should be expected at low temperature, which is in disagreement with the ferromagnetic signal observed in the magnetometry measurements. A possible origin for this ferromagnetic signal is the existence of a non-negligible single-ion magnetic anisotropy for the Co(II) ions, which can produce a non-collinear magnetic structure. In order to investigate this possibility we computed the value of the zero-field

10.1002/chem.201703140

splitting D tensor for the two different Co(II) ions by *ab initio* calculations (see experimental section).

The main results of the *ab initio* calculations for the lowest symmetry space group ($P2_1/n$) are shown in Table 3. In both Co(II) ions, the s = 3/2 ground state multiplet is split up in two doublet states separated by a large energy gap due to a large uniaxial D value. This D value is positive, indicating an easy-plane magnetic anisotropy. In addition, although much smaller than the D value, the non-zero orthorhombic E value shows that there is also a relevant magnetic anisotropy on the easy plane.

In both Co(II) ions the hard axis is almost along a pseudo S_6 axis of the distorted octahedral environment around the Co(II) ions, pointing towards one formate molecule, whereas the easy axis is almost along the projection of one Co-O bond on the easy plane (see Figure 9). Here, it is interesting to remark that in the unit cell there are two Co(1) ions and two Co(2) ions. The symmetry operations relating the two Co(1) ions, or the two Co(2) ions, do not conserve the orientation of the main single-ion magnetic anisotropy axes, resulting in four different orientations of these axes in the unit cell, two for the Co(1) ions and two for the Co(2) ions.

Table 3. Uniaxial (D) and orthorhombic (E) anisotropy terms. Energy gap between the two lowest doublet states.

ion	Energy gap (K)	D(K)	E(K)
Co(1)	293.9	144.1	8.0
Co(2)	294.3	144.7	8.0

The energies involved in the magnetic interactions must be of the same order of magnitude as the magnetic transition temperature (ca. 15 K). Therefore, due to the large uniaxial (D) magnetic anisotropy values, the magnetic moment of each Co(II) ion should almost lay on its easy magnetic anisotropy plane. A representation of these planes is given in Figure S7a in the supplementary information, where we show the easy magnetic anisotropy axis and the intermediate one for all the Co(II) ions in the unit cell, both of them defining the easy anisotropy plane. Although the four different easy planes are not coplanar, all of them almost contain the *a*-axis (*c*-axis in the orthorhombic phase). Therefore, in the case of no magnetic anisotropy in the easy magnetic plane (E = 0), the magnetic moments should be collinear along the *a*-axis and antiferromagnetic coupled. However, the non-zero magnetic anisotropy in the easy magnetic anisotropy plane (E = 8.0 K) would produce a deviation of the magnetic moments from the *a*-axis towards the easy magnetic anisotropy axis of each Co(II) ion. Taking into account the antiferromagnetic order along the *a*-axis, the previous deviation of the magnetic moment gives rise to a global non-compensated component along the *c*-axis (in the monoclinic space group) (see Figure 9 and Figure S7b in the supplementary information). Moreover, the magnetic components along the *b*-axis would be compensated resulting in a zero magnetic moment along that axis. Therefore, these results are in agreement with both, magnetometry measurements and the refined magnetic structures.

Conclusions

Crystal structure analyses of compound **1** reveal an unreported phase transition from *Pnma* space group at RT (**1A**) to $P2_1/n$ space group (non-standard space group of $P2_1/c$) at low temperature (**1B**). This transition involves slight changes in the orientation of the methylammonium counterions, which are weakly anchored into the cavities, as well as in the Co(II) octahedral environments. These modifications in the structure are associated with the occurrence of an electric phase transition from paraelectric to antiferroelectric state. The studies carried out on powder samples show a notable mixture of orthorhombic and monoclinic phases, even at the lowest temperature (ca. 2K). The different ratios between the phases in the different measurements suggest a dependence with the cooling/warming process. Moreover, the broadening of some reflections after the structural transition denotes an important strain contribution.

Together with the occurrence of weak electric transition, complex **1** presents an overall antiferromagnetic coupling with a long-range magnetic order at about 15 K due to the occurrence of a non-collinear antiferromagnetic structure where magnetic moments are not strictly compensated. Therefore, below 15 K this material shows the coexistence of an antiferroelectric-like behaviour originated from a structural phase transition, non-significantly coupled with the weak ferromagnetism arising from the non-compensation of the non-collinear antiferromagnetic structure of the metal-organic host framework. Even if weak ferromagnetism is commonly attributed to the Dzyaloshinskii-Moriya interaction, the *ab initio* calculations indicate that the single-ion anisotropy of Co(II) ions is the dominant term in this case.

The magnetic reflections in the neutron measurements at 2 K are compatible with *Pn'ma'* and $P2'_1/n'$ magnetic models. The best refined models give rise to magnetic structures where the magnetic moments are antiferromagnetically coupled, with a small non-compensated component of the magnetic moment, in agreement with the *ab initio* calculations. However, the obtained magnetic structures at zero-field are not compatible with the magneto-electric behaviour previously observed on this compound under applied field. Therefore, further works are needed to understand the origin of the magneto-electric coupling under applied magnetic fields.

Experimental Section

Materials

Reagents and solvents used in the synthesis were purchased from commercial sources and used without further purification. Elemental analyses (C, H, N) were performed with an EA 1108 CHNS/0 automatic analyzer.

Synthesis of $[CH_3N_3][Co(COOH)_3]$ (1)

Aqueous solutions of $CoCl_2{\cdot}6H_2O$ (3mL, 0.33 M), CH_3NH_3Cl (3 mL, 0.33 M) and NaHCOO (2 mL, 1.5 M), where mixed together with 8 mL of N-methylformamide ($HCONHCH_3$). The resulting solution was sealed in a

10.1002/chem.201703140

Teflon-lined stainless steel vessel (43 mL), heated at 140 ºC for 3 days under autogenous pressure, and then cooled to room temperature. After slow cooling, prismatic pink crystals of $[CH_3NH_3][Co(COOH)_3]$ suitable for single crystal diffraction were obtained with a yield of about 88%. The crystals were filtered, washed with ethanol (10 mL) and dried at room temperature. Anal. Calcd for $C_4H_9CoNO_6$ (%): C, 21.24; H, 4.01; N, 6.20; Found (%). C, 21.37; H, 4.10; N, 6.22. FT-IR (cm^{-1}): υ(N–H): 3118(sh) and 3025(br), υ(CH_3): 2968(w), 1456(m) and 1418(m), υ(C–H): 2875(m) and 2779(w), υ(NH): 2610(w) and 2490(w), υ(OCO): 1567(s) and 1554(s), υ(OCO): 1353(s), 1067(w), υ(C–N): 1000(m) and 971(m), υ(OCO): 807(s) (see details in the supplementary information, see Figure S8).

Dielectric Measurements

Dielectric measurements were performed by measuring the complex impedance of a 4 mm diameter pressed pellet with a thickness of around 300 μm, made from selected ground single crystals using a commercial Agilent E4980 LCR-meter. Four coaxial cables linked to the electronic devices allow the measurements of the complex impedance. In order to extract the dielectric permittivity constant proportional to the capacitance of the sample, we used a model of capacitor and resistance in parallel. Metallic electrodes were formed using silver paste on the parallel faces of the pellet. The best conditions of measurement ruling out extrinsic effects, established by systematic checks of the amplitude and frequency dependence, gives rise to an amplitude voltage of 1 V and a frequency of 10 kHz for the temperature range from 5 to 250 K. The relative permittivity as function of T was measured with a heating/cooling rate of 5 K/min

Heat Capacity

Physical Properties Measurement System (PPMS) from Quantum Design, was used to measure the heat capacity on a single crystal sample. We mounted the sample on a standard sample holder with a small amount of grease. The signal produced for this amount of grease was subtracted in the final data.

Powder X-ray Diffraction Measurements

Powder diffraction measurements were collected on the BL04-MSPD high-resolution powder diffraction beamline at ALBA synchrotron (Barcelona, Spain), equipped with a 13-channel Si(111) multianalyzer detector with high-angular resolution and a helium-based cryostat. We used a ∅ 0.7 mm glass cylinder as sample holder. Two data sets in the 1-59.5º range in 2θ were collected at 135 and 45 K, above and below the crystallographic phase transition, with a wavelength of 0.4948 Å. The data analysis was carried out using the FullProf Suite.[16]

Neutron Powder Diffraction Measurements

Neutron powder diffraction experiments were performed on the high-intensity diffractometer D1B equipped with variable temperature environment at the Institut Laue Langevin (ILL, Grenoble, France). The sample was contained in a ∅6 mm cylindrical vanadium can and placed inside an Orange Cryostat. The diffraction patterns were recorded using λ = 2.52 Å wavelength, above and below the magnetic order temperature, at 20 and 2 K, respectively. Moreover, a thermodiffractogram in the 2-300 K ranges has been collected in order to obtain a global temperature dependence of the sample. The data fits as well as the magnetic structure calculations were carried out using the FullProf Suite of programs.[16]

Single Crystal X-ray Structure Determination and Refinement

Single crystal X-ray diffraction at 300 and 45 K was performed on the CRISTAL beamline at SOLEIL synchrotron (Saclay, France) with λ = 0.67165 Å equipped with a helium stream. A single ϕ-scan was collected at 300 K to check the crystal structure before the phase transition. At low temperature, a combination of ϕ- and ω-scans was collected in order to increase the data completeness. After decreasing the temperature, the crystal suffers a structural phase transition and became into a multiple component twin (**1B**). The indexing and integration protocol implemented in *CrysAlis Pro* program,[17] permitted to obtain a reasonable model of the RT (**1A**) and the low temperature (**1B**) phases. The structures of both phases were solved by direct methods using the SHELXS97 program.[18] All non-hydrogen atoms were refined anisotropically by full-matrix least-squares technique based on F^2 using SHELXL97. The hydrogen atoms were positioned geometrically and refined using the difference electron density map. The final geometrical calculations and the graphical manipulations were carried out with PARST95,[19] PLATON[20] and DIAMOND[21] programs.

At 45 K, the reflections for two different components of the twin were indexed, integrated and scaled. A reconstruction of the reciprocal space plane (*h* 1 *l*) above and below the phase transition is shown in Figure S9 in the supplementary information.

Neutron Single Crystal Diffraction Measurements

In order to properly establish the hydrogen bond network within the **1A** and **1B** structures, a single crystal of about 36 mm³ of compound **1** (see Figure S10 in the supplementary information) was mounted onto a displex system in 4 circle configuration on the monochromatic neutron thermal diffractometer D19 at the Institut Laue Langevin (ILL). We measured the sample at three different temperatures (RT, 135K and 45K) in order to characterize the different structural phases. To solve the structures in the orthorhombic phase at RT and 135K, we collected data using a wavelength of 0.949Å. However, at lower temperatures, reflections from two different twin domains appear and, in order to separate properly the reflections, we change the wavelength to 1.454 Å. The measurement strategy consists on several omega (ω) scans with steps of 0.07° at different χ and φ positions. The Multi-Detector Acquisition Data Software (MAD) from ILL was used for data collection. Unit cell determinations were done by using PFIND and DIRAX programs, and processing of the raw data was applied using RETREAT and RAFD19 programs. Absorption correction was applied using D19ABS program. The structures at RT and 135 K were solved by direct methods using SHELXL. Full matrix least squares refinement on $|F^2|$ using SHELXL-2014/76 as implemented in WINGX program was used for structure refinement, while at 45 K the refinement was performed with JANA2006 program.[22] In the twinned phase each domain contributes 50% to the total intensity and they are related by a rotation of 180º around the *a**-axis. It should be noted that is the same twin-law observed in the single crystal X-ray experiments. After this measurement, the crystal was warmed up and the phase **1A** was recovered without any evidence of damage in the sample.

All atoms could be refined with anisotropic displacement parameters by full-matrix least-squares technique based on F^2. The program Diamond[21] was used for graphical representations. The crystallographic details of the two phases (above and below the structural phase transition), including space groups, lattice parameters as well as some details of the data refinement, are shown in Table 4. Crystallographic data, in CIF format, for the structure of **1A** and **1B** have been deposited at the Cambridge Crystallographic Data Centre with CCDC reference numbers xxxxxxxx and xxxxxxxx.

Table 4. Crystal data and details of the structure determination with neutron diffraction for the complex **1A-1B**

Compound	**1A**			**1B**	
Formula	$C_4H_9CoNO_6$			$C_4H_9CoNO_6$	
M	226.05			226.05	
Crystal system	Orthorhombic			Monoclinic	
Space group	*Pnma*			$P2_1/n$	
Radiation	*X-rays*	*Neutrons*		*X-rays*	*Neutrons*
T(K)	RT	RT	135(2)	45(2)	45(2)
a, Å	8.40770(10)	8.3940(2)	8.2827(2)	8.1750(3)	8.1621(3)
b, Å	11.7215(4)	11.7181(3)	11.6735(2)	8.2710(3)	8.2487(3)
c, Å	8.11090(10)	8.1068(2)	8.1543(2)	11.6730(5)	11.6584(4)
β, deg	-	-	-	91.883(3)	91.891(3)
V, $Å^3$	799.34(3)	797.40(3)	788.42(3)	788.85(7)	784.49(5)
Z	4	4	4	4	4
ρ_{calc} (Mg m^{-3})	1.878	1.883	1.904	1.903	1.914
λ (Å)	0.67165	0.94905	0.94905	0.67165	1.454
μ (mm^{-1})	1.746	0.03884	0.03884	1.769	0.03884
R_1, $I > 2\sigma(I)$ (all)	0.0289 (0.0311)	0.0502 (0.0752)	0.0341 (0.0371)	0.0415 (0.0781)	0.0848 (0.0893)
wR_2, $I > 2\sigma(I)$ (all)	0.0810 (0.0849)	0.1351 (0.1435)	0.0806 (0.0821)	0.0940 (0.1023)	0.1235 (0.1243)
Absorption Correction	Multi-scan	Numerical	Numerical	Multi-scan	Numerical
Independent reflections	1228	2703	2413	3006	1980

Ab Initio Calculations

The *ab initio* calculations were performed using the CASSCF/NEVPT2 method,[23] as implemented in the ORCA quantum chemistry package[24]. After the CASSCF/NEVPT2 computation, the *spin–orbit* and the *spin–spin* coupling relativistic effects, which are at the origin of the magnetic anisotropy, have also been taken into account in the final step. The *ab initio* calculations, for determining the single-ion anisotropy, were done on a quantum cluster of atoms obtained from the experimental X-ray structure at 45 K. Each cluster contains the studied Co(II) ion plus 18 methylammonium and 8 formate neighbour molecules. In addition, six diamagnetic Zn(II) ions were included in the position of the six neighbour Co(II) ions. This quantum cluster was embedded in a field of point charges fitted to reproduce the Madelung field in the cluster region due to the rest of the crystal. The basis sets were the def-TZVP one for the Co(II) ions and the six neighbour formate molecules and the def-SVP one for all the other atoms.

In the CASSCF calculations the active space consisted on the Co(II) 3d orbitals containing 7 electrons (CASSCF(7,5)). The state-averaged CASSCF calculations were done for the six lower energy quartet roots since preliminary tests (with a SVP basis set and without the NEVPT2 energy correction) indicated that higher energy quartet roots or any doublet root have no relevant contribution to the final ground-state multiplet. Then, the NEVPT2 calculations were performed with the CASSCF(7,5) reference space for the treatment of the dynamical correlation energy. After that, the effect of the *spin-orbit* coupling is taken into account using a mean-field operator, which is diagonalized in the basis of the previous CASSCF wavefunctions.

Finally, the computation and diagonalization of the D tensor allows to express the single-ion magnetic anisotropy spin operator for the i^{th} Co(II) ion with an uniaxial and an orthorhombic term:

$$H_i^{single-aniso} = -DS_{iz}^2 + E(S_{ix}^2 - S_{iy}^2) \quad (3)$$

where *ix*, *iy* and *iz* are the main single-ion magnetic anisotropy axes for the i^{th} Co(II) ion.

Acknowledgements

Partial funding for this work is provided by the Ministerio Español de Ciencia e Innovación through projects MAT2015-68200-C02-2-P and the Centro Universitario de la Defensa de Zaragoza through CUD 2013-17 and CUD 2015-20 projects. The authors thankfully acknowledge the resources from the supercomputer "Caesaraugusta" (node of the Spanish Supercomputer Network), technical expertise and assistance provided by BIFI – Universidad de Zaragoza. The use of the physical measurements instruments of Servicio General de Apoyo a la Investigación-SAI, Universidad de Zaragoza is also acknowledged. We acknowledge SOLEIL for provision of synchrotron radiation facilities and we would like to thank Dr. Pierre Fertey for assistance in using the CRISTAL beamline. We are grateful to the Institut Laue Langevin and Spanish-CRG instruments for the allocated neutron beam-time.

Keywords: Multiferroic Materials • Metal-Organic Compounds • Magnetic Structure • Neutron Diffraction • Order-Disorder Phase Transitions

[1] see for example: a) C. Janiak, *Dalton Trans.*, **2003**, 2781 -2804; b) O. M. Yaghi, M. O'Keeffe, N. W. Ockwig, H. K. Chae, M. Eddaoudi, J. Kim, *Nature* **2003**, *423*, 705-714; c) S. Kitagawa, R. Kitaura, S.-I. Noro, *Angew. Chem. Int. Ed.* **2004**, *43*, 2334-2375; d) *Chem. Rev. Special Issue of "Metal Organic Frameworks"* H.-C. Zhou, J. R. Long, O. M. Yaghi Editors, **2012**, *112*, 673-674; e) N. L. Rosi, J. Eckert, M. Eddaoudi, D. T. Vodak, J. Kim, M. O'Keeffe, O. M. Yaghi *Science*, **2003**, *300*, 1127-1129; f) J. S. Seo, D. Whang, H. Lee, S. I. Jun, J. Oh, Y. J. Jeon, K. Kim, *Nature* **2000**, *404*, 982-986; g) L. E. Kreno, K. Leong, O. K. Farha, M. Allendorf, R. P. Van Duyne, J. T. Hupp, *Chem. Rev.*, **2012**, *112(2)*, 1105-1125; h) D. Farrusseng, S. Aguado, C. Pinel, *Angew. Chem. Int. Ed.* **2009**, *48*, 7502-7513; i) A. Lan, K. Li, H. Wu, D. H. Olson, T. J. Emge, W. Ki, M. Hong, J. Li, *Angew. Chem. Int. Ed.* **2009**, *48*, 2334-2338.

[2] a) R. I. Thomson, P. Jain, A. K. Cheetham, M. A. Carpenter, *Physical Review B* **2012,** *86*, 214304-1-214304-7; b) B. Liu, R. Shang, K. L. Hu, Z. M. Wang, S. Gao, *Inorg. Chem.*, **2012**, *51*, 13363-13372; c) J.-C. Tan, P. Jain, A. K. Cheetham, *Dalton Trans.*, **2012**, *41*, 3949-3952; d) A. Stroppa, P. Barone, P. Jain, J. M. Perez-Mato, S. Picozzi, *Adv. Mater.* **2013**, *25*, 2284-2290; e) A. O. Polyakov, A. H. Arkenbout, J. Baas, G. R. Blake, A. Meetsma, A. Caretta, P. H. M. van Loosdrecht, T. T. M. Palstra, *Chem. Mater.* **2012**, *24*, 133-139; f) A. Stroppa, P. Jain, P. Barone, M. Marsman, J. M. Perez- Mato, A. K. Cheetham, H. W. Kroto, S. Picozzi, *Angew. Chem. Int. Ed.* **2011**, *50*, 5847-5850; g) M. Guo, H.-L. Cai, R.-G. Xiong, *Inorg. Chem. Com.* **2010,** *13*, 1590-1598; h) G. Rogez, N. Viart, M. Drillon, *Angew. Chem. Int. Ed.* **2010**, *49*, 1921-1923; i) P. Jain, V. Ramachandran, R. J. Clark, H. D. Zhou, B. H. Toby, N. S. Dalal, H. W. Kroto, A. K. Cheetham, *J. Am. Chem. Soc.*, **2009**, *131*, 13625-13627; j) D.-W. Fu, W. Zhang, H.-L. Cai, Y. Zhang, J.-Z. Ge, R.-G. Xiong, S. D. Huang, T. Nakamura, *Angew. Chem. Int. Ed.* **2011**, *50*, 11947-11951.

[3] Y.-H. Chu, L. W. Martin, M. B. Holcomb, M. Gajek, S.-J. Han, Q. He, N. Balke, C.-H. Yang, D. Lee, W. Hu, Q. Zhan, P.-L. Yang, A. Fraile-Rodríguez, A. Scholl, S. X. Wang, R. Ramesh, *Nat. Mater.* **2008**, *7*, 478-482.

[4] M. Azuma, K. Takata, T. Saito, S. Ishiwata, Y. Shimakawa, M. Takano, *J. Am. Chem. Soc.* **2005**, *127*, 8889-8892.

[5] a) R. Ramesh, *Nature* **2009**, *46*, 1218-1219. b) E. Pardo, C. Train, H. B. Liu, L. M. Chamoreau, B. Dkhil, K. Boubekeur, F. Lloret, K. Nakatani, H. Tokoro, S. Ohkoshi, M. Verdaguer, *Angew. Chem.* **2012**, *51*, 8356-8360. c) W.-J. Xu, K.-P. Xie, Z.-F. Xiao, W.-X. Zhang, X.-M. Chen, *Crystal Growth& Design* **2016**, *16*, 7212-7217. d) L. C. Gómez-Aguirre, B. Pato-

10.1002/chem.201703140

Doldán, A. Stroppa, S. Yáñez-Vilar, L. Bayarjargal, B. Winkler, S. Castro-García, J. Mira, M. Sánchez-Andújar, M. A. Señarís-Rodríguez, *Inorg. Chem.* **2015**, *54*, 2109-2116. e) M. Maczka, A. Pietraszko, B. Macalik, K, Hermanowicz, *Inorg. Chem.* **2014**, *53*, 787-794. f) M. Mączka, A. Gągor, B. Macalik, A. Pikul, M. Ptak, J. Hanuza. *Inorg. Chem.* **2014**, 53, 457-467. g) G. Kieslich, A. C. Forse, S. Sun, K. T. Butler, S. Kumagai, Y. Wu, M. R. Warren, A. Walsh, C. P. Grey, A. K. Cheetham, *Chem. Mater.* **2016**, *28*, 312-317.

[6] a) W. R. Entley, G. S. Girolami, *Inorg. Chem.*, **1994**, *33*, 5165-5166; b) O. Sato, T. Iyoda, A. Fujishima, K. Hashimoto, *Science*, **1996**, *271*, 49-51; c) S. Ferlay, T. Mallah, R. Ouahès, P. Veillet, M. Verdaguer, *Nature*, **1995**, *378*, 701-703; d) S. Ferlay, T. Mallah, R. Ouahès, P. Veillet, M. Verdaguer, *Inorg. Chem.*, **1999**, *38*, 229-234; e) W. Dong, L.-N. Zhu, H.-B. Song, D.-Z. Liao, Z.-H. Jiang, S.-P. Yan, P. Cheng, S. Gao, *Inorg. Chem.*, **2004**, *43*, 2465-2467.

[7] a) Z. Wang, B. Zhang, K. Inoue, H. Fujiwara, T. Otsuka, H. Kobayashi, M. Kurmoo, *Inorg. Chem.* **2007**, *46*, 437- 445. b) G. C. Xu, W. Zhang, X. M. Ma, Y. H. Hen, L. Zhang, H. L. Cai, Z. M. Wang, R. G. Xiong, S. Gao, *J. Am. Chem. Soc.* **2011**, *133*, 14948-14951. c) L. Cañadillas-Delgado, O. Fabelo, J. A. Rodríguez-Velamazan, M.-H. Lemee-Cailleau, S. A. Mason, E. Pardo, F. Lloret, J.-P. Zhao, X.-H. Bu, V. Simonet, C. V. Colin, J. Rodríguez-Carvajal, *J. Am. Chem. Soc.* **2012**, *134*, 19772-19781. d) M. Mączka, A. Gągor, M. Ptak, W. Paraguassu, T. Almeida da Silva, A. Sieradzki, A. Pikul, *Chemistry of Materials* **2017**, *29*, 2264-2275. e) L. Xin, Z. Fan, G. Li, M. Zhang, Y. Han, J. Wang, K.P. Ong, L. Qin, Y. Zheng, X. Lou, *New J. Chem.* **2017**, *41*, 151-159. e) D. Di Sante, A. Stroppa, P. Jain, S. Picozzi, *J. Am. Chem. Soc.* **2013**, *135*, 18126-18130. f) M. Mączka, K. Pasińska, M. Ptak, W. Paraguassu, T. A. da Silva, A. Sieradzki, A. Pikul, *Phys. Chem. Chem. Phys.* **2016**, *18*, 31653-31663. g) M. Mączka, A. Ciupa, A. Gągor, A. Sieradzki, A. Pikul, M. Ptak, *J. Mater. Chem. C*, **2016**, *4*, 1186-1193.

[8] a) F. E. Mabbs, D. J. Machin, *Magnetism and Transition Metal Complexes,* Chapman and Hall, London, 1973; b) B. N. Figgis, M. A. Hitchman, *Ligand Field Theory and its Applications*, Wiley-VCH, New York, 2000; c) D. Armentano, G. de Munno, F. Lloret, M. Julve, *Inorg. Chem.* **1999**, *38*, 3744-3747; d) F. Lloret, M. Julve, J. Cano, R. Ruiz-García, E. Pardo, *Inorg. Chim. Acta.*, **2008**, *361*, 3432-3445.

[9] M. Boca, I. Svoboda, F. Renzc, H. Fuess, *Acta Cryst. Section C: Cryst. Struct. Comm.,* **2004**, *C60*, m631-m633.

[10] L.C. Gómez-Aguirre, B. Pato-Doldán, J. Mira, S. Castro-García, M.A. Señarís-Rodríguez, M. Sánchez-Andújar, J. Singleton, V.S. Zapf, *J. Am. Chem. Soc.* **2016**, *138*, 1122–1125.

[11] M.-Y. Li, B. Liu, B.-W. Wang, Z.-M. Wang, S. Gao, M. Kurmoo, *Dalton Trans.* **2011**, *40*, 6038.

[12] E.I. Stiefel, G.F. Brown, *Inorg. Chem.* **1972**, *11*, 434.

[13] L.J. de Jongh, A.R. Miedema, *Adv. Phys.*, **1974**, *23*, 1.

[14] L. J. De Jongh, Ed. *Magnetic Properties of Layered Transition Metal Compounds*; Kluwer Academic: Dordrecht, The Netherlands, 1990.

[15] E. F. Bertaut, *Magnetism*, vol. III, Ch. 4, G. T. Rado and H. Shul, Eds.; Academic Press, New York, 1963.

[16] J. Rodriguez-Carvajal, *Physica B*, **1993**, *192*, 55. The programs of the FullProf Suite can be obtained at http://www.ill.eu/sites/fullprof.

[17] Agilent. *CrysAlis PRO* Agilent Technologies Ltd, Yarnton, England, 2010.

[18] G. M. Sheldrick, *Acta Cryst.* **2008**, *A64*, 112.

[19] M. Nardelli, *J. Appl. Crystallogr.* **1995**, *28*, 659.

[20] A. L. Spek, *J. Appl. Cryst.* **2003**, *36*, 7.

[21] *DIAMOND 2.1d*, Crystal Impact GbR, CRYSTAL IMPACT, K. Brandenburg & H. Putz GbR, Postfach 1251, D-53002 Bonn, Germany, **2000**.

[22] V. Petricek, M. Dusek, L. *Z.* Palatinus, *Kristallogr.* **2014**, *229(5)*, 345-352. DOI 10.1515/zkri-2014-1737.

[23] D. Ganyushin, F. Neese, *J. Chem. Phys.* **2006**, *125*, 024103.

[24] F. Neese, Wiley Interdiscip. *Rev. Comput. Mol. Sci.* **2012**, *2*, 73.

Entry for the Table of Contents (Please choose one layout)

Layout 1:

FULL PAPER

The structural and magnetic phase transitions and dielectric properties show that $[CH_3NH_3][Co(COOH)_3]$ compound presents a multiferroic behaviour at zero-field. The paraelectric to antiferroelectric-like transition observed at *ca.* 90 K, coexist with a weak ferromagnetic signal below ca. 15 K, which arise from a non-collinear antiferromagnetic structure, mainly due to the single-ion anisotropy of the Co(II) ions.

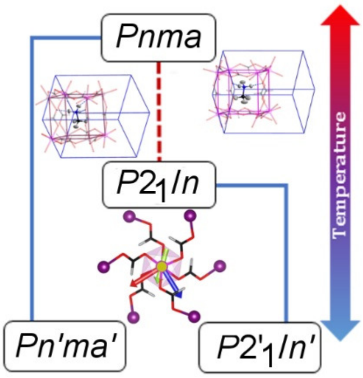

Lidia Mazzuca, Laura Cañadillas-Delgado, Oscar Fabelo,* J. Alberto Rodríguez-Velamaz Javier Luzón, Oriol Vallcorba, Virginie Simone Claire V. Colin, Juan Rodríguez-Carvajal.*

Page No. – Page No.

Microscopic Insights on the Multiferroic Perovskite-like $[CH_3NH_3][Co(COOH)_3]$ Compound